Eng. Sci., 2025, 38, 1851

Engineered Science
DOI: https://dx.doi.org/10.30919/es1851

A Hybrid Method for Scattering of Electrically Large Thick Cavity with Complex Terminal

Yi Zhu, Gao Wei, Xiangwei Liu, Kuisong Zheng, Changying Wu and Jianzhou Li*

Abstract

In this paper, an equivalent source shooting and bouncing ray (ES-SBR) method is proposed to combine with Method of Moments (MoM) for scattering of electrically large thick cavity with complex terminal. The hybrid is achieved by plane wave expansion (PWE) and the generalized reciprocity integral (GRI) method. Different from the traditional SBR method, the far-field integral formula of the ES-SBR method is established by equivalent source to ensure the consistency of scatterings from the exterior cavity and the interior cavity. In contrast to the existing method limited to thin and deep cavity, the proposed ES-SBR-MoM method is applicable for arbitrary shape cavities. Due to the reusability of PWE scattering matrix, the proposed ES-SBR-MoM method greatly improves the efficiency of cavity scattering analysis and has great application prospect in the rapid design of low scattering cavity.

Keywords: Cavity scattering; Plane wave expansion; Generalized reciprocity integral; Equivalent source shooting and bouncing ray.

Received: 25 July 2025; Revised: 11 October 2025; Accepted: 20 October 2025.
Article type: Research article.

1. Introduction

The scattering characteristics analysis of electrically large cavity is a research hotspot in recent years. Various approaches have been presented, including asymptotic methods and full-wave methods. The asymptotic methods mainly refer to the shooting and bouncing ray (SBR) method and the iterative physical optics (IPO) method,[1-4] which are efficient but not accurate. The full-wave methods, such as method of moment (MoM) and finite element method (FEM),[5-7] can provide sufficient accuracy, but they are inefficient for electrically large targets.

In order to balance efficiency and accuracy, extensive in-depth research has been conducted.[8-11] The most common practice is to divide the cavity into an interior region and an exterior region for treatment respectively, which includes two schemes: One is using the same electromagnetic method with different accuracy for the two regions,[12-15] and the other is using different electromagnetic methods for the two regions.[16-18] The latter is more suitable for electrically large cavities, since large and smooth region is handled efficiently by asymptotic method. In particular, the method in Ref. [18] has great advantages in rapid calculation, since the reusable plane wave expansion (PWE) matrix was adopted. However, only the scattering of the interior cavity was studied in Ref. [18], which limited this method to thin cavity. Besides, in order to reduce computational cost through zoning, the thin cavity must be deep.

In this paper, a further study is conducted for electrically large thick cavity. An interface Σ divides the cavities into two parts. The terminal part inside the interface Σ is the interior cavity, and the rest is the exterior cavity. The scattering of the interior cavity is characterized by the PWE scattering matrix and the generalized reciprocity integral (GRI) method,[18] which assumes an external current source and an external observer in far zone. Because the traditional SBR method cannot be combined with the GRI method, the equivalent source shooting and bouncing ray (ES-SBR) method is proposed to process the scattering of the exterior cavity, which adopt a new far-field integral formula to ensure the superposition of the scatterings. The rays are divided into two types. The rays reaching the interface Σ are used to connect the front section of the cavity and the interior cavity. The other rays are used to get the scattering of the exterior cavity. In contrast to the limitation of thin and deep cavity in Ref. [18],

---

School of Electronics and Information, Northwestern Polytechnical University, Xi'an, Shaanxi, 710072, China
*Email: ljz@nwpu.edu.cn (J. Li)

the proposed method can handle variable shape thick cavities with arbitrary depth. Different from the traditional SBR-MoM hybrid methods,[19,20] which deal with the coupling between the SBR region and MoM region through near field, the proposed ES-SBR-MoM hybrid method deals with the coupling between two regions through PWE, which is more accurate and efficient for the cavity, since the multiple reflections in the cavity makes the near field difficult to obtain accurately. The accuracy and efficiency of the proposed ES-SBR-MoM method are proved by several numerical results.

2. Formulation

As shown in Figs. 1(a) and (b), the interface divides the cavities into the interior cavity and the exterior cavity. The scattering is also divided into the contribution of the interior cavity and the exterior cavity. The PWE and the GRI method for handling interior cavity is described in Section 2.1. The exterior cavity is processed by the ES-SBR method as shown in Section 2.2.

2.1 Scattering of the interior cavity

As shown in Fig. 2, the cavity is excited by a plane wave generated by current source $\vec{J}(P)$ at point P in far zone. The interface Σ is completely contained by a square of width $2a$ at the $z=0$ plane. According to the GRI method, the scattering field of the interior cavity at point P can be expressed by Eq. (1):[21]

$$\vec{E}^{s}_{interior}(P)\cdot\hat{p} \approx \int_{S}(\vec{E}^{s}\times\vec{H}^{i}-\vec{E}^{i}\times\vec{H}^{s})\cdot\hat{z}ds \tag{1}$$

where $\vec{E}^{s}_{interior}(P)$ is the scattering field of the interior cavity, $\hat{p}$ denote the direction of $\vec{J}(P)$. $(\vec{E}^{s},\vec{H}^{s})$ and $(\vec{E}^{i},\vec{H}^{i})$ are the scattering field and the incident field at Σ, respectively.

In K-space, the electric field $\vec{E}$ and the magnetic field $\vec{H}$ can be expanded into:

$$\begin{Bmatrix}\vec{E}(x,y,z)\\ \vec{H}(x,y,z)\end{Bmatrix}=\frac{1}{4\pi^{2}}\int_{-\infty}^{\infty}\int_{-\infty}^{\infty}\begin{Bmatrix}\vec{f}(k_x,k_y)\\ \vec{g}(k_x,k_y)\end{Bmatrix}e^{-j\vec{k}\cdot\vec{r}}dk_xdk_y \tag{2}$$

where $(\vec{E},\vec{H})$ and $(\vec{f},\vec{g})$ are two pairs of Fourier transforms, $\vec{k}=k_x\hat{x}+k_y\hat{y}+k_z\hat{z}$. The spectrum $(\vec{f},\vec{g})$ on Σ can be regarded as a bandlimited signal within a square of width $2a$. According to the sampling theorem, the spectrum can be completely specified by its samples when the sampling interval Δk is not larger than π/a. So, taking π/a as the sampling interval, Eq. (2) can be discretized into the following form:[18]

$$\begin{Bmatrix}\vec{E}(x,y,0)\\ \vec{H}(x,y,0)\end{Bmatrix}=\frac{1}{4a^{2}}\sum_{-\infty}^{\infty}\sum_{-\infty}^{\infty}\begin{Bmatrix}\vec{f}(m,n)\\ \vec{g}(m,n)\end{Bmatrix}e^{-j\vec{k}(m,n)\cdot\vec{\rho}} \tag{3}$$

where $\vec{f}(m,n)$ and $\vec{g}(m,n)$ are the PWE coefficients, and

$$\vec{\rho}=x\hat{x}+y\hat{y}\,,\ k_x(m,n)=\frac{m\pi}{a}\,,\ k_y(m,n)=\frac{n\pi}{a}\,,$$

$$k_z(m,n)=\sqrt{k^{2}-\left(\frac{m\pi}{a}\right)^{2}-\left(\frac{n\pi}{a}\right)^{2}} \tag{4}$$

According to Eq. (4), for propagating plane waves, (m,n) is truncated by

$$\left(\frac{m\pi}{a}\right)^{2}+\left(\frac{n\pi}{a}\right)^{2}<k^{2} \tag{5}$$

Taking Eq. (3) into Eq. (1),

$$\vec{E}^{s}_{interior}(P)\cdot\hat{p}\approx\frac{1}{4a^{2}}\sum_{m,n}[\vec{f}^{s}(m,n)\times\vec{g}^{i}(m,n)-\vec{f}^{i}(m,n)\times\vec{g}^{s}(m,n)]\cdot\hat{z} \tag{6}$$

According to the orthogonality, Eq. (6) can be further simplified as:[18]

$$\vec{E}^{s}_{interior}(P)\cdot\hat{p}\approx\frac{-1}{2a^{2}\eta}\sum_{m.n}\vec{f}^{i}(m,n)\cdot\vec{f}^{s}(m,n)\cos\theta^{s} \tag{7}$$

where η is the impedance of free space. $\vec{f}^{i}(m,n)$ and $\vec{f}^{s}(m,n)$ represent the incident PWE coefficient and the scattering PWE coefficient, respectively. $\cos\theta^{s}$ is defined by (m,n).

$\vec{f}^{i}(m,n)$ is determined by ray tracing in this paper. Rays are divided into quadrilateral ray tubes on an initial incident surface as shown in Fig. 2. It assumes that there are J effective rays tube reaching the interface Σ. $\vec{f}^{i}(m,n)$ can be determined by the inverse Fourier transform corresponding to Eq. (2).

$$\begin{Bmatrix}f_x^{i}(m,n)\\ f_y^{i}(m,n)\end{Bmatrix}=\sum_{j=1}^{J}\iint_{\Delta x_j\Delta y_j}\begin{Bmatrix}E_x(x_j,y_j,0)\\ E_y(x_j,y_j,0)\end{Bmatrix}e^{jk_0\left[(u-s_x)x+(v-s_y)y\right]}e^{jk_0\left(s_xx_j+s_yy_j\right)}dxdy \tag{8}$$

where $(\Delta x_j\Delta y_j)$ is the projection area between Σ and the ray tube. $E(x_j,y_j,0)$ is the field of central ray at the intersection $(x_j,y_j,0)$. (s_x,s_y,s_z) is the incident direction at $(x_j,y_j,0)$. $u=\sin\theta^{i}\cos\varphi^{i}$, $v=\sin\theta^{i}\sin\varphi^{i}$. The incident direction (θ^{i},φ^{i}) is decided by (m,n).[18]

$$\begin{gathered}\sin\theta^{i}=\frac{\lambda}{2a}\sqrt{m^{2}+n^{2}},\quad\cos\theta^{i}=\sqrt{1-\sin^{2}\theta}\\ \cos\varphi^{i}=\frac{m}{\sqrt{m^{2}+n^{2}}},\quad\sin\varphi^{i}=\frac{n}{\sqrt{m^{2}+n^{2}}}\end{gathered} \tag{9}$$

When $(m,n)=(0,0)$, (θ^{i},φ^{i}) is set to $(0,0)$. The observation direction (θ^{s},φ^{s}) is determined in the same way. $\vec{f}^{s}(p,q)$ is connected with $\vec{f}^{i}(m,n)$ by the PWE scattering matrix $\bar{\bar{S}}(m,n;p,q)$.[18]

$$\vec{f}^{\,s}(p,q)=\sum_{m,n}\bar{\bar{S}}(m,n;p,q)\vec{f}^{\,i}(m,n) \tag{10}$$

where $\bar{\bar{S}}(m,n;p,q)=\hat{\theta}^s S_{\theta\theta}\hat{\theta}^i+\hat{\theta}^s S_{\theta\varphi}\hat{\varphi}^i+\hat{\varphi}^s S_{\varphi\theta}\hat{\theta}^i+\hat{\varphi}^s S_{\varphi\varphi}\hat{\varphi}^i$. $\vec{f}^{\,i}(m,n)$ is obtained by Eq. (8). According to Eqs. (3) and (10),

$$S_{\alpha\beta}(m,n,p,q)\approx\frac{E^s_{r\alpha}(p,q)\pi}{j2ka^2E^i_{o\beta}(m,n)\cdot\cos\theta^s} \tag{11}$$

where α and β represent one of θ or φ polarization. $E^s_r(p,q)$ is the bistatic scattering field of the interior cavity illuminated by an incident plane wave $E^i(m,n)$. The incident direction and the observation direction are determined by Eq. (5), and Eq. (9).

According to Eq. (11), $\bar{\bar{S}}(m,n;p,q)$ can be obtained by $E^i(m,n)$ and $E^s_r(p,q)$. To ensure accuracy, MoM is used to get the scattered field $E^s_r(p,q)$. Different from the treatment in Ref. [18] which introduce a hemispherical cap on the back end of the termination section, only the grid of the interior cavity is used for MoM in this paper, aiming to minimize the error from the exterior cavity and reduce computational complexity.

2.2 Scattering of the exterior cavity

The ES-SBR method is adopted for the exterior cavity. The electric field on the surface of the exterior cavity is obtained by ray tracing as the traditional SBR method. However, the general far-field integral formula is not applicable since the scattering field of the interior cavity is calculated at external point P in far zone. Therefore, a new far-field integral formula is derived in the ES-SBR method, which calculates the scattering field at point P to ensure superposition.

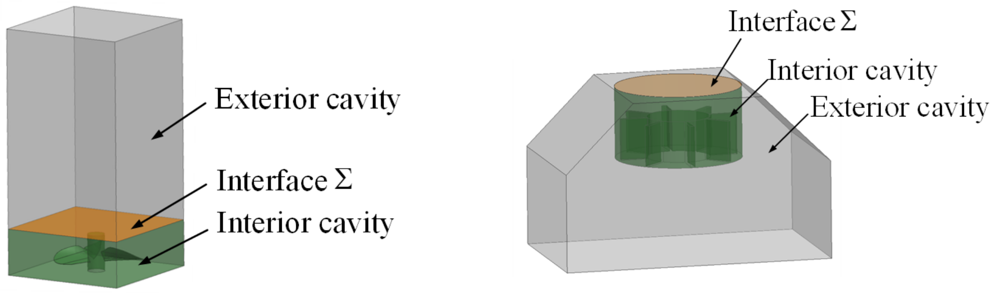

(a) (b)

Fig. 1: Regional division of cavity. (a) A thin and deep cavity is divided into interior cavity and exterior cavity by an interface inside the cavity. (b) A thick and shallow cavity is divided into interior cavity and exterior cavity by an interface at the top of the cavity.

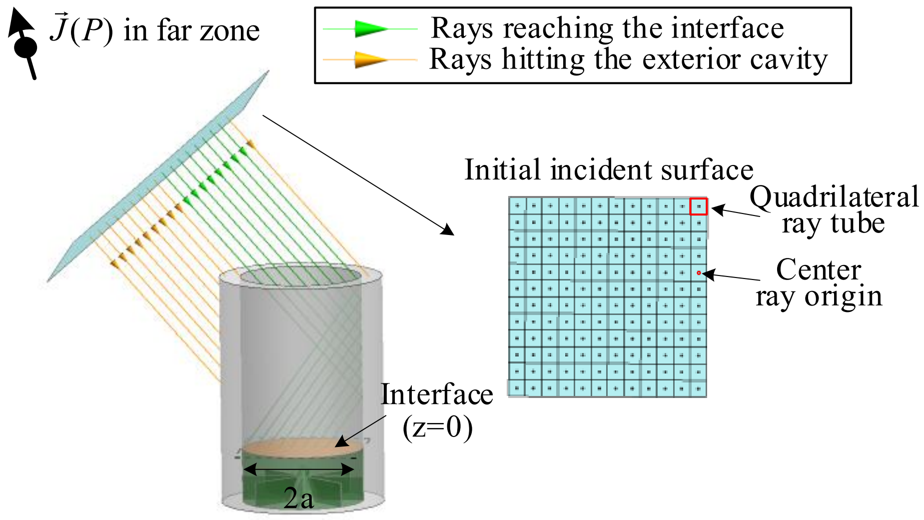

Fig. 2: The incident plane wave generated by a current source $\vec{J}(P)$ in far zone irradiates the cavity, and the quadrilateral ray tube is segmented on an initial incident surface for ray tracing.

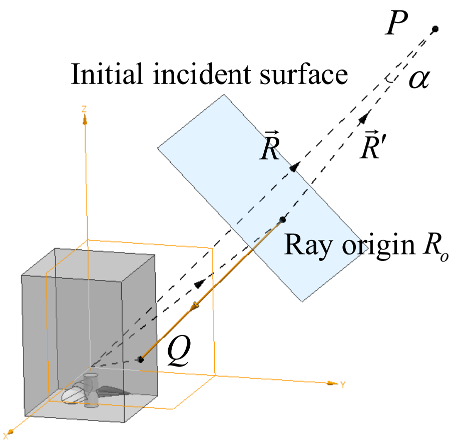

Fig. 3: The vector relationship among the intersection Q, central ray origin R_o, and far zone source point P when a central ray starting from the initial incident surface hits the exterior cavity.

As shown in Fig. 3, a ray with origin at R_o intersects with the exterior cavity at point Q. The equivalent magnetic current $\vec{K}_s$ generated by the surface electric field at point Q is regarded as a new radiation source.

$$\vec{K}_s = 2\vec{E}(Q) \times \hat{n} \tag{12}$$

where $\hat{n}$ is the outside normal at Q. The scattering field at point P generated by the ray tube which centered on this ray can be determined by the new radiation source in Eq. (12).[1]

$$\vec{E}^s_{a\_raytube}(P) = \iint\limits_{\Delta x'\Delta y'} \frac{je^{-jkR}\left[\vec{E}(Q)\times\hat{n}\right]}{\lambda R} e^{-j\vec{k}\cdot\vec{r}'} dx'dy' \tag{13}$$

where $\Delta x'\Delta y'$ is the projection area of the ray tube, R is the distance from the coordinate origin to P. $\vec{r}'$ is the vector from the coordinate origin to point Q.

The initial incident field $\vec{E}^i$ of the ray is generated by a current source at point P, so

$$\vec{E}^i = \frac{j\hat{p}Z_0}{2\lambda R'} e^{-jkR'} \tag{14}$$

where R' is the distance from the ray origin R_o to P.

$$R' = \left|\vec{R} - \vec{R}_o\right| = (R - R_i)\cdot\cos\alpha \approx R - R_i \tag{15}$$

R_i is the distance from the coordinate origin to the initial incident surface. α is the angle between $\vec{R}$ and $\vec{R}'$, $\cos\alpha \approx 1$ since point P is located in far zone.

Taking Eqs. (14) and (15) into Eq. (13), the scattering field of the ray tube at point P can be calculated by a new far-field integral formula, which is not affected by R.

$$\vec{E}^s_{a\_raytube}(P)\cdot\hat{p} = \frac{2e^{-jkR_i}}{\eta} \vec{E}^i \cdot \iint\limits_{\Delta x'\Delta y'} \left[\vec{E}(Q)\times\hat{n}\right] e^{-j\vec{k}\cdot\vec{r}'} dx'dy' \tag{16}$$

The scattering field of the exterior cavity is the superposition of the contributions of all the exterior effective ray tubes.

$$\vec{E}^s_{exterior}(P)\cdot\hat{p} = \sum_{l=1}^{L} \vec{E}^s_{a\_raytube}(P)\cdot\hat{p} \tag{17}$$

where L is the number of the exterior effective ray tubes.

The monostatic radar cross section (RCS) of the whole cavity is defined as

$$\sigma = \lim_{R\to\infty} 4\pi R^2 \frac{\left|\vec{E}^s_{interior}(P)\cdot\hat{p} + \vec{E}^s_{exterior}(P)\cdot\hat{p}\right|^2}{\left|\vec{E}^i\right|^2} \tag{18}$$

where $\vec{E}^s_{interior}(P)\cdot\hat{p}$ and $\vec{E}^s_{exterior}(P)\cdot\hat{p}$ are determined by Eq. (7), Eq. (16), and Eq. (17). R can be eliminated by Eq. (14),[18] so Eq. (18) can be simplified as:

$$\sigma = \frac{(k\eta)^2}{4\pi} \frac{\left|\vec{E}^s_{interior}(P)\cdot\hat{p} + \vec{E}^s_{exterior}(P)\cdot\hat{p}\right|^2}{\left|\vec{E}^i\right|^4} \tag{19}$$

According to Eq. (19), the monostatic RCS of the whole cavity can be obtained directly from the scattering of the interior cavity and the exterior cavity at point P.

3. Simulations and discussion

The following five simulation examples will be used to investigate the accuracy and efficiency of the proposed ES-SBR-MoM method. The results of all examples are simulated on a workstation equipped with two Intel Xeon CPU Gold-6248R and 512G RAM. The results of MoM in Altair Feko are used as reference to demonstrate the accuracy and efficiency of the proposed hybrid method. All models are meshed by triangular facets. For MoM region, the side length of triangular facets is 0.2λ. For ES-SBR region, two different side length of triangular facets are used. When the cavity is planar, the side length is set to 0.5λ; When the cavity is curved, the side length is set to 0.1λ for ensuring the accuracy of ray tracing.

3.1 Thick rectangular cavity

To illustrate the correctness of the proposed far-field integral formula, the proposed hybrid method is compared with the ES-SBR method. As the thick rectangular cavity shown in Fig. 4(a), the interface is 3.5λ away from the bottom, $a = 4\lambda$, $\Delta k = \pi / a$. The frequency is 3GHz. Fig. 4(b) shows the monostatic RCS of $\theta\theta$ polarization, at $\varphi = 0°$, $\theta = 0° - 90°$. The comparison of the real part and imaginary part of the scattering electric fields are shown in Figs. 4(c) and (d), respectively. The coincidence of the curves in Figs. 4(c) and (d) verifies the correctness of the proposed far-field integral formula, which means that the scattering electric fields from the ES-SBR

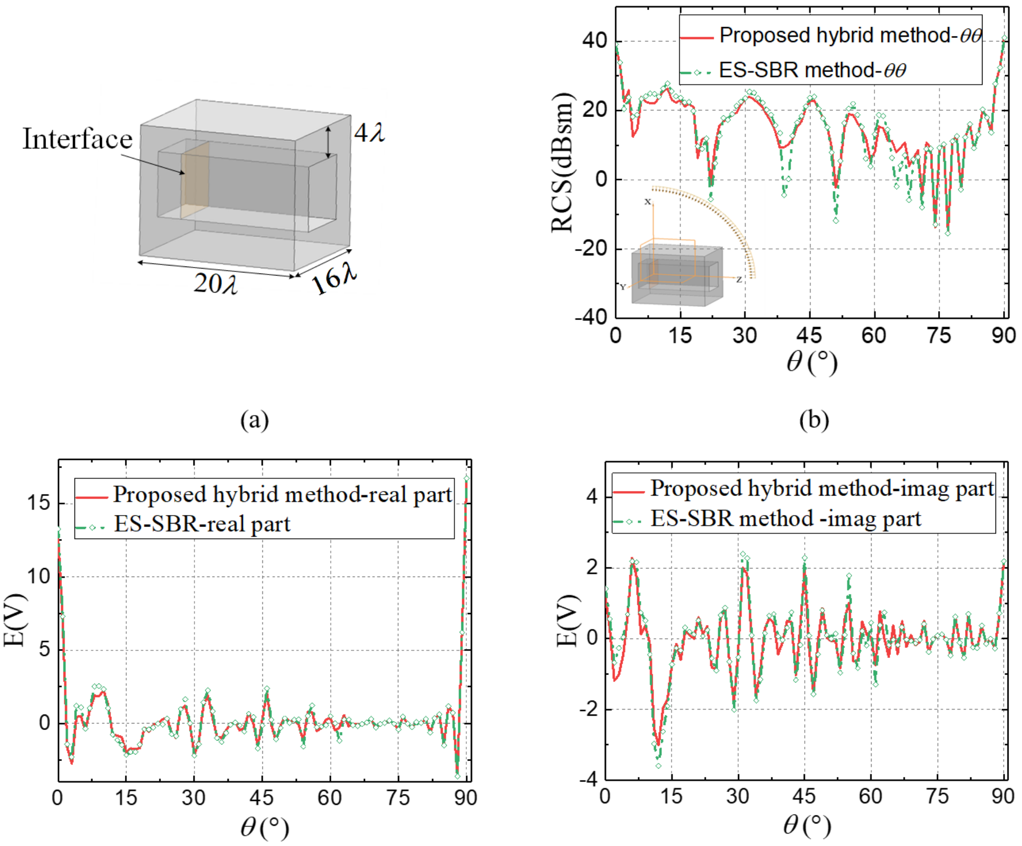

(a) (b)

(c) (d)

Fig. 4: Thick rectangular cavity. (a) Dimensions of the thick rectangular cavity. (b) $\theta\theta$ polarized monostatic RCS of the thick rectangular cavity. (c) Real part of the scattering electric field. (d) Imaginary part of the scattering electric field.

method and the GRI method are received at the same point and stackable.

3.2 Cylindrical cavity

As shown in Fig. 5(a), a cylindrical cavity is used to analysis the influence of interface position. The interface is set at 8λ, 10λ, and 12λ away from the bottom of the cavity, respectively. $a = 5\lambda$, $\Delta k = \pi / a$. The $\theta\theta$ polarized RCS of the proposed hybrid method is compared with that of the MoM. The frequency is 3GHz. The incident angle varies in the range of $\theta = -90° - 90°$ for $\varphi = 0°$. It can be seen from Fig. 5(b) that all results are in good agreement especially for small incident angles. For large incident angle, the results of proposed hybrid method mainly depend on the SBR method, which does not consider the influence of edges, resulting in poor agreement at $\theta = -50° - -70°$ and $\theta = 50° - 70°$. Comparing the results of the proposed hybrid method when the interface is at different positions, it can be seen that the interface position has little effect on the results. The computational time and memory

Table 1: Computational time and memory consumption of cylindrical cavity.

Model	Method		Grids number of MoM region	Memory (GB)	Time (min)
Cylindrical cavity	MoM		116698	154.68	91.62
	Proposed method with different interface position	8λ	24051	16.48	34.08
		10λ	27565	20.59	45.50
		12λ	31241	28.59	61.68
	Proposed method with different grid density	0.25λ	24051	14.32	30.25
		0.1λ		16.48	34.08
		0.05λ		18.66	47.67

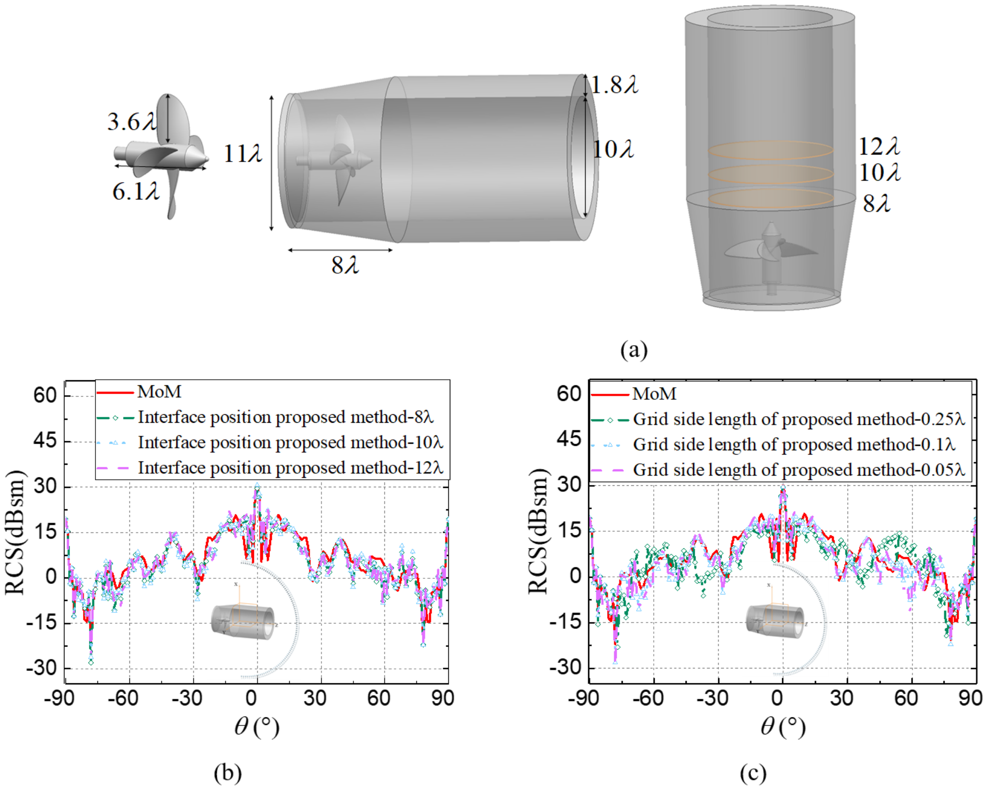

(a)

(b) (c)

Fig. 5: Cylindrical cavity. (a) Dimensions of cylindrical cavity. (b) $\theta\theta$ polarized monostatic RCS of different interface position. (c) $\theta\theta$ polarized monostatic RCS of different grid side length.

consumption are shown in Table 1. It is better to set the interface closer to the complex terminal based on the computational complexity.

Considering that cylindrical cavity is sensitive to grid density, triangular facets of different sizes are used to divide the cavity. Fig. 5(c) shows the $\theta\theta$ polarized RCS comparison when the side lengths of triangular facets are 0.25λ, 0.1λ and 0.05λ, respectively. The corresponding grid number for ray tracing is 74568, 468684, and 1871938, respectively. The interface is 8λ away from the bottom of the cavity. When the side length is 0.25λ, the curve coincides poorly since the inaccurate tracing caused by multiple reflections. When the side length is 0.1λ and 0.05λ, the curves coincide well with that of MoM. The computational costs are shown in Table 1. Considering both efficiency and accuracy, it is better to set the side length of triangular facets to 0.1λ for curved cavity.

3.3 Rectangular cavity with complex terminal

The proposed method is also applicable to thin cavity. As shown in Fig. 6(a), a spiral blade is located at the bottom of a thin rectangular cavity. The interface is 3.5λ away from the bottom. To analyze the influence of the sampling interval, the results from the proposed method at different sampling interval are compared with that of MoM. Fig. 6(c) shows the sample of angles on the *xoy* plane at different sampling interval. The operating frequency is set to 3GHz. Fig. 6(b) shows the monostatic RCS of $\varphi\varphi$ polarizations, at $\varphi = 0°$, $\theta = 0° - 90°$. The trends of all curves are basically consistent. The results at $\Delta k = k/10$ and $\Delta k = k/12$ agree better with the reference one at $50° - 60°$ than the results at $\Delta k = k/8$, while the agreement is worse at small incident angles since more samples will bring greater cumulative error. Therefore, smaller sampling interval does not help improve the overall accuracy. Considering both computational complexity and accuracy, $\Delta k = \pi / a$ is the optimal sampling interval.

To verify the reusability of the PWE scattering matrix, the cavity in Fig. 6(a) is modified as shown in Fig. 6(d). The proposed method adopts the existing PWE scattering matrix obtained with sampling interval of $\Delta k = \pi / a$. Fig. 6(e) shows the monostatic RCS comparison between the proposed method and MoM. The agreement of the results demonstrates the accuracy of the proposed method and the reusability of the PWE scattering matrix.

The computational time and memory consumption comparison between the proposed method and MoM are shown in Table 2. The computational time and memory consumption of the proposed method is quite lower than that of MoM since only the interior cavity used MoM. Besides, due to the repeated use of PWE scattering matrix, the computational time and

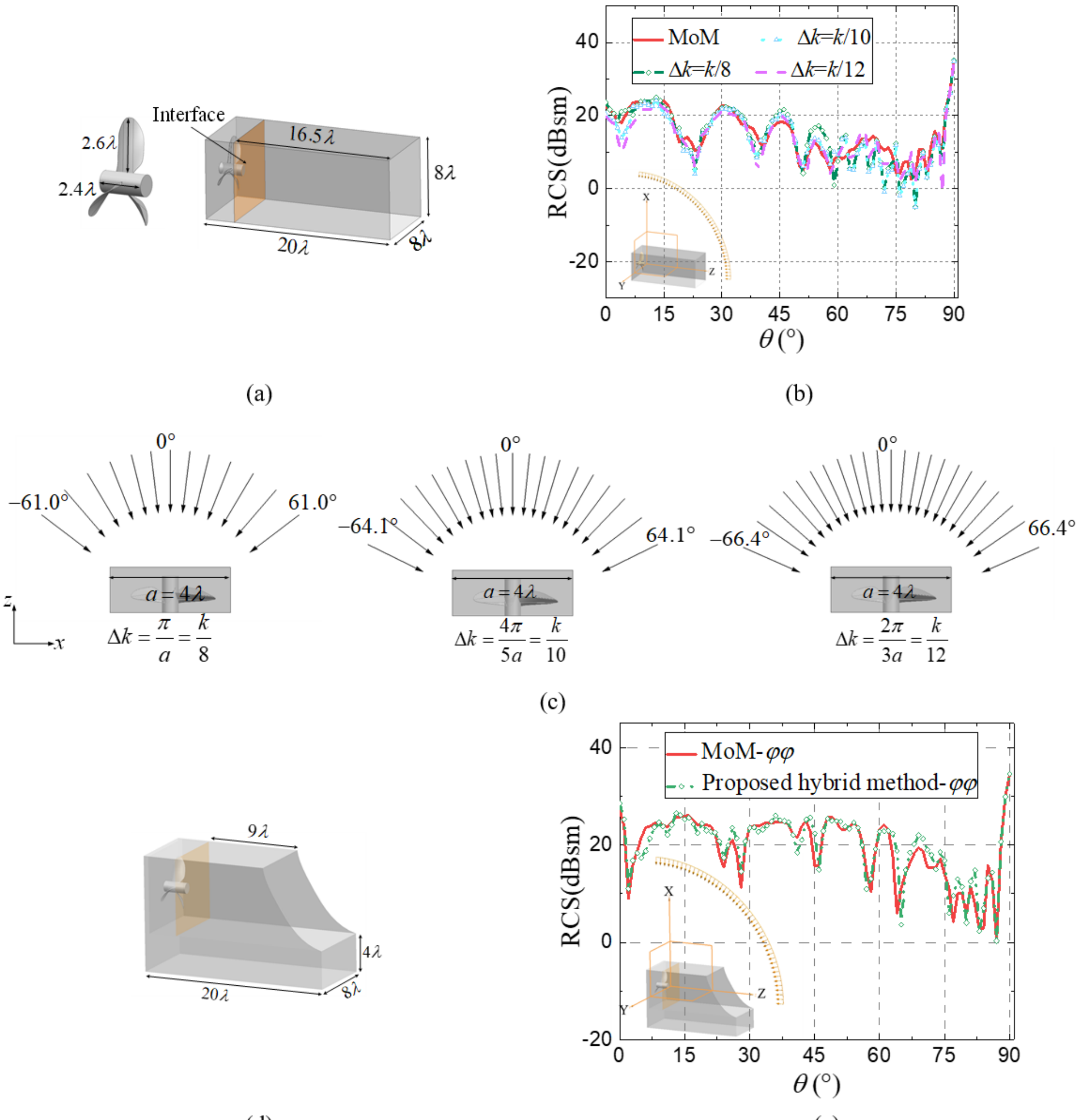

(a) (b)

(c)

(d) (e)

Fig. 6: Rectangular cavity with complex terminal. (a) Dimensions of the thin rectangular cavity. (b) $\varphi\varphi$ polarized monostatic RCS of the thin rectangular cavity. (c) The sample of angles on the *xoy* plane at different sampling interval. (d) Dimensions of the modified rectangular cavity. (d) $\varphi\varphi$ polarized monostatic RCS of the modified rectangular cavity.

Table 2: Computational time and memory consumption of rectangular cavity with complex terminal.

Model	Method		Grids number of MoM region	Memory (GB)	Time (min)
Thin rectangular cavity	MoM		83950	118.40	51.50
	Proposed method with different sampling interval	$\Delta k=\pi/a$	11876	3.36	8.27
		$\Delta k=4\pi/5a$		4.64	11.20
		$\Delta k=2\pi/3a$		6.25	15.67
Modified rectangular cavity	MoM		82162	112.84	47.32
	Proposed method		N.A.	0.58	2.68

Note: N.A. means that MoM is not required since the PWE scattering matrix has already been obtained.

memory consumption of the proposed method is extremely low for modified rectangular cavity. This comparison shows the superiority of the proposed method in multiple calculations.

3.4 Thick and shallow cavity

As shown in Fig. 7(a), the cavity is used to verify the accuracy and efficiency of the proposed method for thick and shallow cavity. The interface is set to the top of the cavity. The operating frequency is set to 1GHz. $a = 5\lambda$, $\Delta k = \pi / a$. The monostatic RCS of $\theta\theta$ polarization and $\varphi\varphi$ polarization at $\varphi = 0°$, $\theta = -45° - 45°$ are shown in Figs. 7(c) and (d), respectively. The curves are derived from the proposed method, MoM and the method in Ref. [18]. The MoM region of the method in Ref. [18] only included the interior cavity here. It can be seen that the RCS of the proposed method and MoM are in good agreement for both polarizations, while the results of the method in Ref. [18] are inconsistent with the other two since the influence from the exterior cavity is nonnegligible. The error between the method in Ref. [18] and MoM is about 8dB at $\theta = 0°$, while the error between the proposed hybrid method and MoM is about 0.2dB. The computational time and memory consumption of the three methods are shown in Table 3. The efficiency of the hybrid method is significantly higher than that of MoM. The efficiency of the proposed method is almost the same as that of the method in Ref. [18], since ray tracing is not a time-consuming process compared to MoM. These results demonstrate the accuracy, universality, and efficiency of the proposed method.

3.5 Irregular cavity

An irregular cavity is used to further validate the reusability of PWE scattering matrix and the accuracy of the proposed method. As shown in Fig. 8(a), the cavity transitions uniformly from the polygon at the front end to the circle at the end. The interface is set to the top of the cavity. The operating frequency is 3GHz. $a = 5.5\lambda$, $\Delta k = \pi / a$. Fig. 8(b) shows the monostatic RCS of $\theta\theta$ polarization, at $\varphi = 0°$, $\theta = 0° - 45°$. The RCS of the proposed method and MoM are in good agreement, while the RCS of the SBR method is inconsistent with the other two, which demonstrates that the accuracy of the proposed method is higher than the SBR method. To verify the reusability of the PWE scattering matrix for irregular front section, a modified irregular cavity was used as shown in Fig. 8(c). Fig. 8(d) shows the monostatic RCS of $\theta\theta$ polarization at $\varphi = 0°,\ \theta = 0° - 45°$. The result of the proposed method still matches that of MoM much better than the SBR method. The computational time and memory consumption of the three methods are shown in Table 4. These results further illustrate the advantages of the proposed method in accuracy and efficiency.

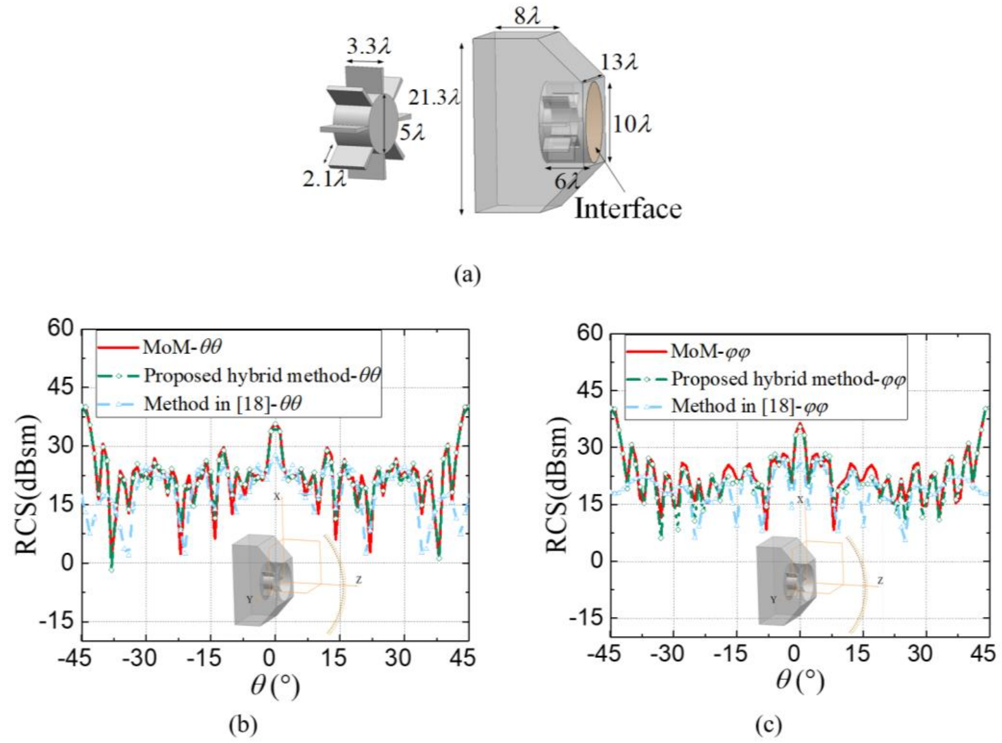

(a)

(b)

(c)

Fig. 7: Thick and shallow cavity. (a) Dimensions of the cavity. (b) $\theta\theta$ polarized monostatic RCS of the cavity. (c) $\varphi\varphi$ polarized monostatic RCS of the cavity.

Table 3: Computational time and memory consumption of thick and shallow cavity.

Model	Method	Grids number of MoM region	Memory (GB)		Time (min)	
			$\theta\theta$	$\varphi\varphi$	$\theta\theta$	$\varphi\varphi$
Thick and shallow cavity	MoM	96404	289.32	295.66	136.50	140.33
	Proposed method	24219	15.03	14.86	30.85	29.45
	Method in [18]	24219	14.33	14.80	29.83	28.89

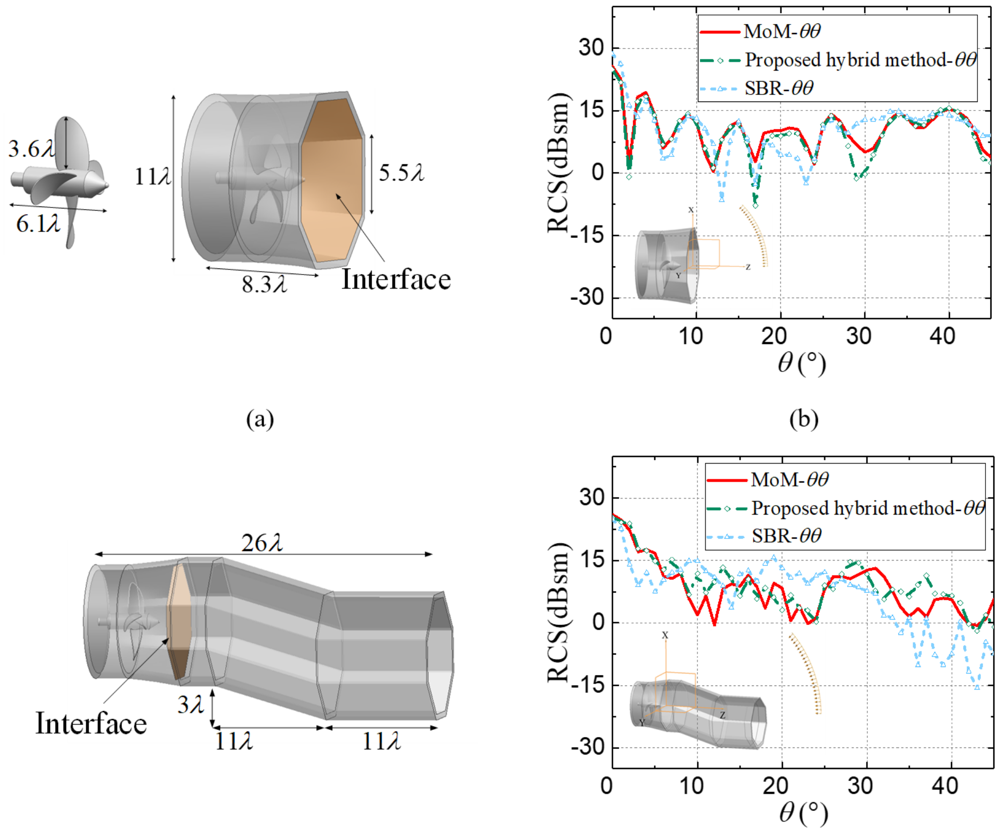

(a) (b)

(c) (d)

Fig. 8: Irregular cavity. (a) Dimensions of the irregular cavity. (b) $\theta\theta$ polarized monostatic RCS of the irregular cavity. (c) Dimensions of the modified irregular cavity. (d) $\theta\theta$ polarized monostatic RCS of the modified irregular cavity.

Table 4: Computational time and memory consumption of irregular cavity.

Model	Method	Grids number of MoM region	Memory (GB)	Time (min)
Irregular cavity	MoM	49212	40.77	28.32
	Proposed method	25487	11.97	25.78
	SBR	N.A.	0.42	0.92
Modified irregular cavity	MoM	160906	513.33	248.75
	Proposed method	N.A.	1.03	4.85
	SBR	N.A.	0.89	1.43

Table 5: Efficiency comparison between the proposed method and MoM.

Model	MoM (min)	Proposed method (min)	Speedup
Thin rectangular cavity	51.50	8.27	6.23×
Modified rectangular cavity	47.32	2.68	17.66×
Irregular cavity	28.32	25.78	1.10×
Modified irregular cavity	248.75	4.85	51.29×

The acceleration performance of example 3.3 and example 3.5 is summarized in Table 5. Due to the reusability of the PWE scattering matrix, the efficiency of the proposed method for the modified model is quite high.

4. Conclusion

A hybrid method considering both efficiency and accuracy is presented for electrically large thick cavity in this paper. The proposed method adopts the PWE scattering matrix in Ref. [18] and extends it to arbitrary cavity, which greatly improves the applicability. In contrast to other hybrid methods, the proposed method has significant advantages in multiple calculations with the help of the PWE scattering matrix. Numerical results show that the efficiency of the proposed method is much higher than that of MoM while ensuring high accuracy. Due to the high efficiency and the reusability of PWE scattering matrix, the proposed method has great application prospects in the rapid design of low scattering cavity.

Conflict of Interest

There is no conflict of interest.

Supporting Information

Not applicable.

CRediT Statement

Yi Zhu: Writing – Original draft, Resources, Methodology, Investigation. **Gao Wei**: Project administration, Investigation, Data curation. **Xiangwei Liu**: Supervision, Software. **Kuisong Zheng**: Supervision, Resources. **Changying Wu**: Supervision, Resources. **Jianzhou Li**: Writing – review & editing, Supervision, Resources.

References

[1] H. Ling, R. C. Chou, S. W. Lee, Shooting and bouncing rays: calculating the RCS of an arbitrarily shaped cavity, *IEEE Transactions on Antennas and Propagation*, 1989, **37**, 194-205, doi: 10.1109/8.18706.

[2] Y. Zhu, G. Wei, J. Li, A shooting and bouncing ray method for electrically large targets with nonuniform thickness anisotropic material, *IEEE Transactions on Antennas and Propagation*, 2024, **72**, 6156-6161, doi: 10.1109/TAP.2024.3407346.

[3] F. Obelleiro-Basteiro, J. Luis Rodriguez, R. J. Burkholder, An iterative physical optics approach for analyzing the electromagnetic scattering by large open-ended cavities, *IEEE Transactions on Antennas and Propagation*, 1995, **43**, 356-361, doi: 10.1109/8.376032.

[4] M. A. Shah, Ç. Tokgöz, B. A. Salau, Radar cross section prediction using iterative physical optics with physical theory of diffraction, *IEEE Transactions on Antennas and Propagation*, 2022, **70**, 4683-4690, doi: 10.1109/TAP.2021.3137202.

[5] S. Rao, D. Wilton, A. Glisson, Electromagnetic scattering by surfaces of arbitrary shape, *IEEE Transactions on Antennas and Propagation*, 1982, **30**, 409-418, doi: 10.1109/TAP.1982.1142818.

[6] L. Zhang, N. Yuan, M. Zhang, L. W. Li, Y. B. Gan, RCS computation for a large array of waveguide slots with finite wall thickness using the MoM accelerated by P-FFT algorithm, *IEEE Transactions on Antennas and Propagation*, 2005, **53**, 3101-3105, doi: 10.1109/TAP.2005.854537.

[7] J. M. Jin, Chapter 2, The Finite Element Method in Electromagnetics. 3rd ed, Wiley, IEEE Press, Hoboken, NJ, USA, 2014, 23-52, ISBN: 9781118571361.

[8] H. T. Anastassiu, A review of electromagnetic scattering analysis for inlets, cavities, and open ducts, *IEEE Antennas and Propagation Magazine*, 2003, **45**, 27-40, doi: 10.1109/MAP.2003.1282177.

[9] J. Liu, J. Jin, Scattering analysis of a large body with deep cavities, *IEEE Transactions on Antennas and Propagation*, 2003, **51**, 1157-1167, doi: 10.1109/TAP.2003.812280.

[10] K. Zhang, C. Wang, J. Jin, Broadband monostatic RCS and ISAR computation of large and deep open cavities, *IEEE Transactions on Antennas and Propagation*, 2018, **66**, 4180-4193, doi: 10.1109/TAP.2018.2841423.

[11] I. Kim, H. R. Im, I. P. Hong, H. Lee, J. G. Yook, An accelerated method of a generalized transition matrix model using characteristic basis functions for large-scale open-ended cavities, *IEEE Transactions on Antennas and Propagation*, 2024, **72**, 6813-6818.

[12] F. Hu, C. Wang, Preconditioned formulation of FE-BI equations with domain decomposition method for calculation of electromagnetic scattering from cavities, *IEEE Transactions on Antennas and Propagation*, 2009, **57**, 2506-2511, doi: 10.1109/TAP.2009.2024579.

[13] J. Hu, R. Zhao, M. Tian, H. Zhao, M. Jiang, X. Wei, Z. P. Nie, Domain decomposition method based on integral equation for solution of scattering from very thin, conducting cavity, *IEEE Transactions on Antennas and Propagation*, 2014, **62**, 5344-5348, doi: 10.1109/TAP.2014.2341701.

[14] Y. Hu, G. Xiao, S. Xiang, A generalized transition matrix model combined with discontinuous Galerkin method for open cavities, *IEEE Open Journal of Antennas and Propagation*, 2020, **1**, 272-282, doi: 10.1109/OJAP.2020.2999657.

[15] S. Xiang, G. Xiao, J. Mao, A generalized transition matrix model for open-ended cavity with complex internal structures, *IEEE Transactions on Antennas and Propagation*, 2016, **64**, 3920-3930, doi: 10.1109/TAP.2016.2583067.

[16] T. Chia, R. J. Burkholder, R. Lee, The application of FDTD

in hybrid methods for cavity scattering analysis, *IEEE Transactions on Antennas and Propagation*, 1995, **43**, 1082-1090, doi: 10.1109/8.467644.

[17] J. Jin, S. S. Ni, S. Lee, Hybridization of SBR and FEM for scattering by large bodies with cracks and cavities, *IEEE Transactions on Antennas and Propagation*, 1995, **43**, 1130-1139, doi: 10.1109/8.467650.

[18] P. R. Rousseau, R. J. Burkholder, A hybrid approach for calculating the scattering from obstacles within large, open cavities, *IEEE Transactions on Antennas and Propagation*, 1995, **43**, 1068-1075, doi: 10.1109/8.467642.

[19] X. Mei, Y. Zhang, H. Lin, A new efficient hybrid SBR/MoM technique for scattering analysis of complex large structures, *2015 IEEE International Conference on Computational Electromagnetics*, February 2-5, Hong Kong, China, IEEE, 2015, 306-308, doi: 10.1109/COMPEM.2015.7052643.

[20] T. Fan, L. Guo, W. Liu, A novel OpenGL-based MoM/SBR hybrid method for radiation pattern analysis of an antenna above an electrically large complicated platform, *IEEE Transactions on Antennas and Propagation*, 2016, **64**, 201-209, doi: 10.1109/TAP.2015.2500218.

[21] P. H. Pathak, R. J. Burkholder, A reciprocity formulation for the EM scattering by an obstacle within a large open cavity, *IEEE Transactions on Microwave Theory and Techniques*, 1993, **41**, 702-707, doi: 10.1109/22.231668.

Open Access